



Enhanced nitrogen photofixation on Fe-doped TiO₂ with highly exposed (1 0 1) facets in the presence of ethanol as scavenger

Weirong Zhao*, Jing Zhang, Xi Zhu, Meng Zhang, Jing Tang, Min Tan, Yan Wang

Department of Environmental Engineering, Zhejiang University, Hangzhou 310058, China

ARTICLE INFO

Article history:

Received 8 February 2013

Received in revised form 13 July 2013

Accepted 21 July 2013

Available online 29 July 2013

Keywords:

Electron transfer

Photocatalytic reduction

Titanate nanotube

Electrochemical impedance spectroscopy

Density functional theory

ABSTRACT

To enhance nitrogen photofixation more effectively, Fe-doped TiO₂ nanoparticles with highly exposed (1 0 1) facets were prepared successfully by two-step hydrothermal method. The quantum yield of nitrogen photofixation in the presence of ethanol as scavenger can be significantly enhanced to $18.27 \times 10^{-2} \text{ m}^{-2}$ which is 3.84 times higher than pristine TiO₂. The electrochemical properties of the photocatalyst reveal that the improvement of photocatalytic activity can be attributed to the enhancement of charge carrier's concentration and photocurrent density by the optimal doping of Fe³⁺. The electron spin-resonance spectroscopy demonstrates the generation of active radicals such as $\cdot\text{O}_2^-$ and $\cdot\text{OH}$ in the nitrogen photofixation. The quantum yields of nitrogen photofixation depend on the partial pressure of nitrogen in the reaction. A systematic experimental investigation accompanying with periodic density functional theory calculation into the intermediates reveals the intrinsic electron transfer pathways and the mechanism of nitrogen photofixation. The entire reduction process of 1 mol N₂ to 2 mol NH₃ with consumption of 6 mol electrons on TiO₂ is similar to the traditional biological nitrogen fixation process. The proposed electron transfer mechanism may be useful to other applications, which use semiconductor materials as photocatalysts.

© 2013 Elsevier B.V. All rights reserved.

1. Introduction

The life of all living organisms relies on the natural nitrogen fixation by some soil-dwelling bacteria or the artificial fixation by the Haber-Bosch process under high pressure and temperature [1,2]. Nitrogen fixation as the second most important chemical process in nature next to photosynthesis [3] is difficult to occur naturally because it is energy intensive. Among the various technologies, photocatalytic production of ammonia has attracted much attention because TiO₂ is chemically inert, photostable, inexpensive, and non-toxic. The nitrogen photofixation under UV irradiation of Fe-doped TiO₂ powder has been first reported by Schrauzer and Guth [4]. Subsequently, some attempts were made two decades ago based on bulk materials of TiO₂ semiconductors [5–7]. Most of the studies on nitrogen photofixation have focused on metal modified TiO₂. The activity of nitrogen photofixation of TiO₂ can be improved by doping of Fe³⁺ and the enhancement was attributed to appropriate Fe³⁺ concentration [7]. Dai et al. [8] revealed that introducing of Fe³⁺ as impurity can inhibit the recombination of photogenerated electron-hole pairs, and consequently enhance the photocatalytic activity. Linnik and Kisch [9] proposed an electron transfer

mechanism of iron titanate (Fe₂TiO₅) thin film on nitrogen photofixation in the presence of ethanol and traces of oxygen [3]. However, the ammonia concentrations of these studies are still in a very low range from 1 to 10 μM due to the low electron transfer activity of Fe-doped TiO₂ prepared. There is no report focusing on the transfer of photogenerated electrons, holes, and active radicals on the surface of Fe-doped TiO₂. The mechanism of ammonia synthesis on Fe-doped TiO₂, including intermediates, adsorption forms, and the kinetics of the reaction have not been explained as well.

Furthermore, the surface of anatase TiO₂ is dominated by the thermodynamically stable (1 0 1) facets [10,11], while the conventional understanding is that the anatase TiO₂ (0 0 1) facets are especially active [12]. Interestingly, many researchers [13–16] revealed that (1 0 1) facets exhibited higher reactivity than (0 0 1) facets. According to the ab initio density functional theory (DFT) calculations, Wu et al. [17] testified that the exposed (1 0 1) facets yielded an enhanced activity with molecular oxygen, facilitating the generation of superoxide radical $\cdot\text{O}_2^-$.

In this study, based on a simple hydrothermal route, titanate nanotubes (TNTs) in hydrogen titanate (H₂Ti₃O₇) phases were prepared via ion exchange method with synthesized nanotubes of sodium tri-titanate (Na₂Ti₃O₇). By using TNTs as precursor to adsorb Fe³⁺, which has large specific surface areas and distinct ion exchange capability [18,19], we reported an iron ion evenly

* Corresponding author. Tel.: +86 571 8898 2032, fax: +86 571 8898 2032.

E-mail addresses: weirong@mail.hz.zj.cn, weirong@zju.edu.cn (W. Zhao).

doped anatase TiO₂ with highly exposed (1 0 1) facets prepared by hydrothermal method. Photocatalytic activity of the photocatalysts was evaluated by nitrogen photofixation under UV light irradiation of 254 nm. Electrochemical methods were employed to demonstrate the effect of Fe³⁺ doping on charge carriers concentration and photocurrent density in photocatalysts. By using electron spin-resonance spectroscopy (ESR) technique to explore the nature of generated radicals such as •O₂⁻, •OH, and CH₃•CHOH, the transfer of photogenerated electron–hole pairs and active radicals in nitrogen photofixation process were investigated. Furthermore, a possible mechanism of the nitrogen photofixation was proposed and the relationship between the electrochemical properties and photocatalytic activity was also discussed.

2. Experimental

2.1. Photocatalyst preparation

TNTs were prepared by hydrothermal method as follows: 1.5 g TiO₂ (P25, Degussa) powder was mixed with 70 mL of 10 M NaOH solution and the obtained mixed solution was stirred for 3 h. The mixture was then heated at 160 °C for 48 h in a 100 mL Teflon-lined autoclave. After hydrothermal reaction, the precipitate of Na₂Ti₃O₇ phases was filtrated and washed with 0.1 M HCl solution until the pH value of the rinsing solution reached ca. 7.0 to acquire H₂Ti₃O₇. The precipitate of H₂Ti₃O₇ phases was washed by deionized water to remove excess Cl⁻ until the conductivity of rinsing solution is below 2 μS cm⁻¹. The washed samples were dried at 80 °C for 8 h to obtain TNTs.

The preparation of Fe-doped TiO₂ nanoparticles was as follows: 1.5 g as-prepared TNTs were mixed with 40 mL deionized water. The pH value of the suspensions was adjusted to 1.5 with 4.0 M HCl to prevent the hydrolysis of Fe³⁺. A series of 1 mL FeCl₃ solutions with various concentrations were added to the mixed solution in drops with stirring. The nominal atomic ratios of Fe to Ti in the precursors are 0, 10, 50, 100, 200, and 500 × 10⁻⁶, and the samples are labeled as S₀, S₁₀, S₅₀, S₁₀₀, S₂₀₀, and S₅₀₀, respectively. The mixture was stirred for 24 h to ensure that Fe³⁺ was exchanged on TNTs completely. Then, 14 mL deionized water were added into the mixture slowly with stirring for 2 h. The obtained mixture was transferred into a 100 mL Teflon-lined autoclave and heated at 180 °C for 12 h. The white precipitate was separated by filtration and washed with deionized water until the conductivity of rinsing solution is below 2 μS cm⁻¹. The washed samples were then dried at 80 °C for 1 h to evaporate the water and finally calcined in ambient air at 500 °C for 3 h to yield Fe-doped TiO₂ nanoparticles.

2.2. Material characterization

The quantitative elemental analysis of synthesized Fe-doped TiO₂ nanoparticles were analyzed by inductively coupled plasma-atomic emission spectroscopy (ICP-AES, Atomscan advantage, Thermo Jarrell Ash Corporation, USA). The as-prepared powders were dissolved in K₂S₂O₇ and diluted sulfuric acid; and the solutions were concentrated for analysis if needed. The measurement wavelengths for Ti and Fe are 308.802 and 238.204 nm, respectively.

The synthesized Fe-doped TiO₂ nanoparticles were characterized by transmission electron microscopy (TEM), high-resolution transmission electron microscopy (HRTEM), electron paramagnetic resonance (EPR) spectroscopy, ESR spectroscopy, photoluminescence (PL) spectra, and Brunauer–Emmett–Teller (BET) specific surface area measurements. A Jeol JEM-2010F electron microscope at an accelerating voltage of 200 kV was used for obtaining TEM and HRTEM images of samples. EPR and ESR spectra were recorded

by a Bruker ESRA-300 spectrometer with microwave power of 20.25 mW at the working frequency of 9.86 GHz and modulation amplitude of 1 G at 100 kHz. The samples were irradiated by a UV lamp of 254 nm at room temperature. The PL spectra were measured by a Fluorolog-3-Tau spectrophotometer using a UV lamp of 365 nm as the excitation source. BET specific surface areas (*S*_{BET}) were determined by nitrogen physisorption at 77 K using an automatic analyzer (Autosorb-iQ-MP, Quantachrome, USA) after the samples preheated to 300 °C for 4 h.

2.3. Electrochemical characterization

Electrochemical workstation (CH Instruments 650D, China) with a standard three-electrode quartz cell was used to evaluate the electrochemical properties of the photocatalysts, including a working electrode, a platinum wire used as counter electrode, and an Ag/AgCl electrode used as reference electrode. All electrochemistry experiments were carried out in 0.1 M Na₂SO₄ solution as electrolyte.

The preparation procedures of working electrodes were as follows: 0.1 g photocatalyst was mixed with 1 mL deionized water and 0.05 mL acetyl acetone. Then, the slurry was evenly coated on a 20 × 20 mm indium–tin oxide (ITO) glass electrode with a sheet resistance of 15 Ω and the area of the photocatalyst coated was kept on 1 cm². Finally, the electrode was calcined at 300 °C for 1 h as the working electrode.

A 4-W UV lamp (G4T5 luming, China) emitting of 254 nm was used as the light source. The data of electrochemical impedance spectroscopy (EIS) were obtained in the frequency range from 100 kHz to 0.1 Hz under amplitude of 10 mV in direct current (DC) potential of +0.2 V vs. Ag/AgCl (equivalent to +0.4 V vs. SHE). In the experiment, pure argon gas was introduced into the gas phase of the reactor at a rate of 100 mL min⁻¹ to maintain an anaerobic atmosphere [20]. Nyquist plots were extracted from these experimental data and fitted to a suggested equivalent circuit using ZSimpWin 3.22d program from Echem Software. Mott–Schottky (MS) experiments were performed in a fixed frequency of 100 Hz for a DC potential range from –0.8 to +1.6 V vs. Ag/AgCl with a step of 50 mV. Photocurrent densities vs. time curves were obtained using the same electrochemical cell in the EIS experiments for 50 s in the dark and 100 s under the irradiation of 254 nm with a 4-W UV lamp in three cycles.

2.4. Photocatalytic testing

The nitrogen photofixation experiments were carried out in a double-walled quartz reactor in air. 0.1 g of photocatalyst mixed with 100 mL solution of 0.789 g L⁻¹ ethanol as scavenger was irradiated by a 4-W UV lamp emitting of 254 nm. 3 mL of the reaction solution was sampled periodically. The concentration of ammonia in supernatant was measured using Nessler's reagent spectrophotometry method by a TU-1901 spectrophotometer (Pgeneral, China). The photon absorbed by reactor *I*₀ was determined as 7.06 × 10⁻⁶ Einstein L⁻¹ s⁻¹ by a UV light meter (Sentry ST-512, China).

The intermediates in the reaction solution were investigated by a nano-liquid-chromatography electrospray ionization quadrupole time-of-flight mass spectrometry (Nano-LC ESI Q TOF MS, MS4-APIQSTAR, USA). The electrospray voltage was set to 2500 V at the inlet capillary, nitrogen drying gas at 350 °C and the flow rate of spray desolvation was 4 L min⁻¹. 50 μL of the reaction solution was injected at a flow rate of 25 μL min⁻¹. All the intermediates were investigated in ESI (positive ion mode). The mass spectra were recorded ranging from 5 to 600 m/z.

The quantum yield φ (m⁻²) of nitrogen photofixation was calculated as the ratio of formation rate of ammonia *k* (M s⁻¹) to surface

Table 1
Summary of the physicochemical properties of samples.

Sample	Fe/Ti ^a ($\times 10^6$)	Crystallite size (Å)	S_{BET} ($\text{m}^2 \text{g}^{-1}$)	N_{d} ($\times 10^{-18} \text{cm}^{-3}$)	k ($\times 10^8 \text{M s}^{-1}$)	φ ($\times 10^2 \text{m}^{-2}$)
S_0	3	275	25	4.74	3.08	5.22
S_{10}	14	257	25	6.26	6.72	11.25
S_{50}	55	250	26	6.59	8.12	13.32
S_{100}	106	224	27	9.81	11.80	18.27
S_{200}	192	260	24	5.31	4.73	8.25
S_{500}	488	261	25	5.05	3.11	5.28

^a Atomic ratios.

area S (m^2) of photocatalyst and photon absorbed by reactor I_0 (Einstein $\text{L}^{-1} \text{s}^{-1}$) as

$$\varphi = \frac{3k}{S \times I_0} \quad (1)$$

2.5. Computational methods

All electronic structure calculations were performed using the CASTEP [21,22] package in the Accelrys Materials Studio modeling suite using periodic DFT within the generalized gradient approximation by Perdew, Burke, and Ernzerhof [21]. The anatase TiO_2 (1 0 1) facets surface was chosen to perform DFT simulations because the surface of TiO_2 are highly exposed with (1 0 1) facets, and the atomic ratio of Fe in the Fe-doped TiO_2 is very low. To prevent the interactions between the adsorbate molecule and surface, the slabs were separated from their periodic images in the z -direction by a vacuum space of 15 Å. $p(2 \times 2)$ supercell of TiO_2 (1 0 1) was modeled to prevent the interaction between adsorbate molecules. The electronic states were expanded using plane waves as a basis set with a cutoff of 340 eV, and the Brillouin zone was sampled using a $2 \times 3 \times 1$ Monkhorst–Pack k -grid. The interaction energy of the adsorbate molecule on TiO_2 (1 0 1) was calculated as

$$\Delta E = E(\text{slab} + \text{adsorbate}) - E(\text{slab}) - E(\text{adsorbate}) \quad (2)$$

3. Results and discussion

3.1. Characterization of Fe– TiO_2 nanoparticles

The results of quantitative elemental analysis by ICP–AES indicated that the Fe/Ti atomic ratios in the synthesized powders were very close to the nominal values in the precursors as listed in Table 1. Thus, the Fe/Ti atomic ratios in the synthesized powders are hereafter quoted as those in the precursors.

The diffraction peaks of all samples in the XRD (Fig. S1 in the Supporting Information) can be indexed to the anatase phase of TiO_2 (JCPDS card no.73–1028, tetragonal, space group $I4_1/amd$). The strong peaks of (1 0 1) facets in Fig. S1 infer that the surfaces of all photocatalysts are highly exposed with (1 0 1) facets. There are no characteristic peaks of iron oxides phases like Fe_2TiO_5 or $\alpha\text{-Fe}_2\text{O}_3$ which have poor photocatalytic activity [23].

Raman spectra in Fig. S2 suggest that the nanoparticles of S_0 and S_{100} are composed of anatase. No iron oxide characteristic peaks can be observed in the spectra of S_{100} because of low doping concentrations of Fe^{3+} , which is in accordance with the result of XRD measurement.

Table 1 lists the summary of the physicochemical properties of samples. As can be seen from Table 1, the crystallite sizes of Fe-doped TiO_2 are slight smaller than that of undoped TiO_2 , indicating a weak distortion in the crystal structure. Because the radii of Ti^{4+} (0.68 Å) and Fe^{3+} (0.64 Å) are very close, the Fe^{3+} can substitute the lattice sites of Ti^{4+} to form iron–titanium solid solution [24].

The doping of Fe^{3+} as a kind of crystallographic point defects can restrict the continuous growth of TiO_2 particles. The optimal doping concentration of $100 \times 10^{-6} \text{Fe}^{3+}$ favors the formation of TiO_2 with smallest crystalline size, thus the as-prepared S_{100} is expected to have an enhanced photocatalytic activity. The narrow range of S_{BET} (Table 1) from 24 to $27 \text{m}^2 \text{g}^{-1}$ indicates that the introducing of Fe^{3+} has no obvious effect on the surface area of TiO_2 because of low doping concentrations of Fe^{3+} .

EPR is a highly sensitive spectroscopic technique for examining paramagnetic species and can give valuable information about the lattice site in which a paramagnetic dopant ion is located. This highly sensitive technique can detect concentration of iron ions in metal oxide matrices lower than 100×10^{-6} [25]. Fig. 1 shows the EPR spectra of undoped TiO_2 and $100 \times 10^{-6} \text{Fe}^{3+}$ doped TiO_2 . As shown in Fig. 1, S_{100} shows intense signal at $g = 2.0037$ and weak signal at $g = 4.2646$. According to the previous reports [26,27], this two signals can be attributed to Fe^{3+} substituted for Ti^{4+} in the TiO_2 lattice ($g = 2.0037$) and Fe^{3+} substituted in the lattice adjacent to a charge-compensating oxide anion vacancy ($g = 4.2646$), respectively. Thus, the results confirm that Fe^{3+} ions are successfully incorporated into the crystal lattice of TiO_2 with the two-step hydrothermal method. In this study, the spectra of S_0 do not show any absorption, demonstrating that there are no paramagnetic impurities and defects in undoped TiO_2 .

Fig. 2a and b shows the TEM images of TNTs prepared by hydrothermal reaction, in which TNTs with diameter of 30–40 nm can be clearly observed. Although the detailed structure of TNTs is still under debate, it is currently accepted that TNTs are of layered tri-titanate structure characterized by a typical interlayer distance of ca. 0.9 nm. This interlayer distance is ca. 14 times larger than the diameter of Fe^{3+} (0.64 Å), and Fe^{3+} in solution can be transported to the surface of nanotubes layers and exchange with hydrogen

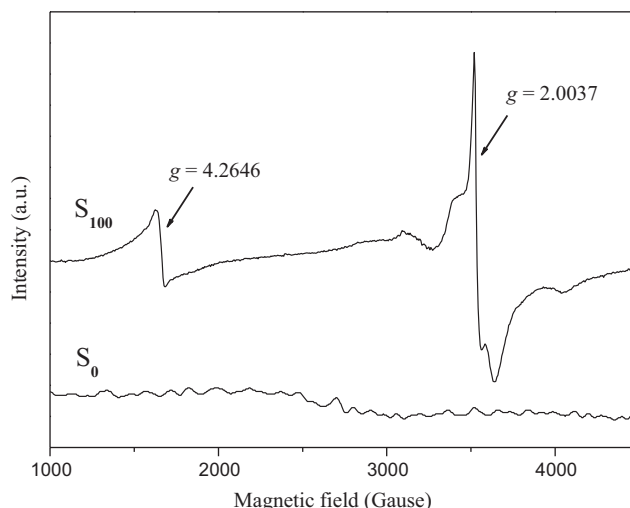


Fig. 1. EPR spectra of undoped TiO_2 (S_0) and $100 \times 10^{-6} \text{Fe}^{3+}$ doped TiO_2 (S_{100}).

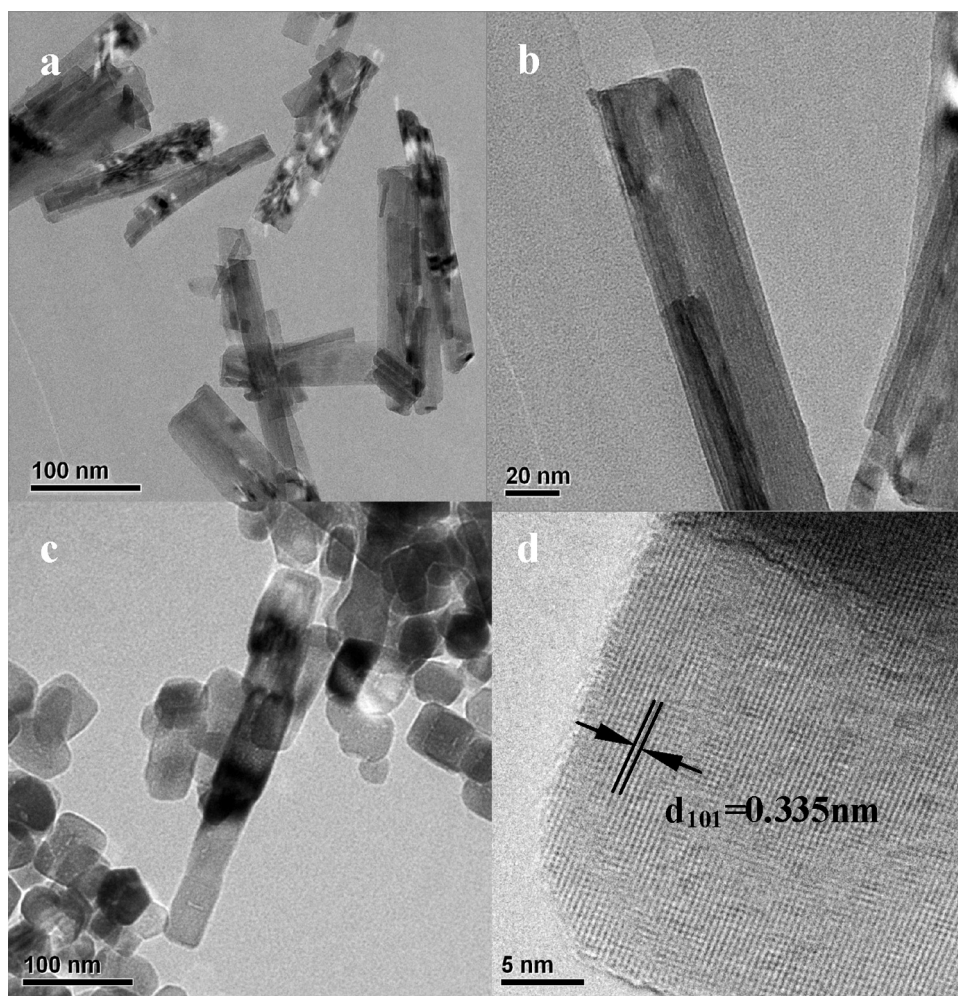


Fig. 2. (a and b) TEM images of titanate nanotubes prepared by hydrothermal reaction. (c) TEM images and (d) HRTEM image of $100 \times 10^{-6} \text{ Fe}^{3+}$ doped TiO_2 (S_{100}).

ion on the surface accordingly. Therefore, the uniform distributing Fe-doped TiO_2 nanoparticles via nanoconfinement effect after another hydrothermal reaction can be obtained [28]. Fig. 2c shows a mixture of square and rod Fe-doped TiO_2 particles in morphology with small diameter of 20–30 nm. HRTEM image of S_{100} shown

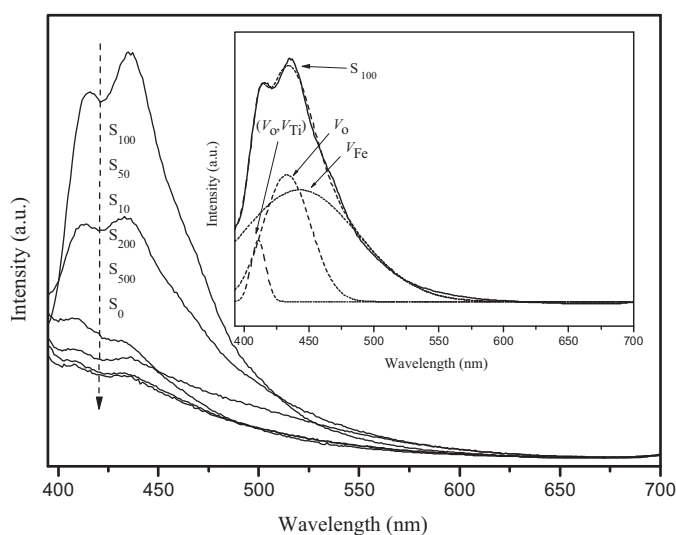
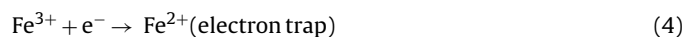


Fig. 3. PL spectra of undoped TiO_2 (S_0) and Fe-doped TiO_2 under the excitation wavelength of 365 nm, and (inset) Gaussian fit of $100 \times 10^{-6} \text{ Fe}^{3+}$ doped TiO_2 (S_{100}).

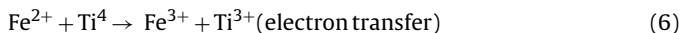
in Fig. 2d indicates that the obtained Fe-doped TiO_2 nanoparticles are mainly of a single crystalline structure with fringe spacing of 0.335 nm corresponding to the (1 0 1) facet.

Fig. 3 shows PL spectra under an excitation wavelength of 365 nm. The sequence of the PL intensity of the photocatalysts is: $S_{100} > S_{50} > S_{10} > S_{200} > S_{500} > S_0$. Strong emissions of S_{50} and S_{100} are observed ranging from 390 to 600 nm with two obvious PL peaks at 408 and 440 nm. It is considered that the PL emission is originated from surface oxygen vacancy and defect due to the doping of Fe^{3+} [29]. The stronger the intensity of PL spectrum is, the higher the contents of surface oxygen vacancies and defects are. Thus, it can be speculated that S_{100} has the richest structural defects and surface oxygen vacancies. The spectra of S_{100} are fitted to Gaussian curves with three peaks at 408, 440, and 450 nm as shown in Fig. 3 (inset). The PL signals at 408, 440, and 450 nm are attributed to the titanium–oxygen vacancy pairs (V_O, V_{Ti}) [30], oxygen vacancies (V_O) [31], and the Fe^{3+} interstices (V_{Fe}), respectively.

A small amount of Fe^{3+} can act as a temporary photo-generated electron or hole trapping site to inhibit the recombination of photo-generated charge carriers with quantum yield φ_0 as [32,33]



Because Fe^{4+} and Fe^{2+} are more unstable than Fe^{3+} [34], there is a strong tendency for the transfer of trapped charges from Fe^{4+} and Fe^{2+} to Fe^{3+} in the photocatalyst surface as



Fe^{3+} not only has effect on the crystal structure, which can directly affect the PL intensity, but also is beneficial for trapping photogenerated electrons and holes to inhibit the recombination of them [35]. The oxygen vacancies on or near the surface of nanoparticles can enhance the adsorption of water and the formation of surface hydroxyl groups, consequently improving the photocatalytic activity [36]. However, when there are excessive doping Fe^{3+} in the photocatalyst, the temporary photogenerated electron or hole-trapping sites will disappear and Fe^{3+} gradually acts as recombination centers [37]. The recombination rate of trapped electrons and holes will increase, consequently decreasing the photocatalytic activity.

Some works [23,24,38] testified that Fe-doping induces the shift of the absorption edge into the visible-light range with the narrowing of the band gap. However, as shown in Fig. S3, the band gap of P25 and Fe-doped TiO_2 can be determined as 3.20 and 3.15 eV, respectively. The doping of Fe^{3+} on Fe-doped TiO_2 in this work has no obvious effect on the E_g because the low doping concentration of Fe^{3+} cannot introduce impurity level to the bandgap of TiO_2 .

3.2. Electrochemical properties of Fe- TiO_2 nanoparticles

A detailed analysis of electrical behavior of undoped and Fe-doped TiO_2 was studied using EIS. According to the data of EIS, an equivalent model based on the model of Roberts and Crowell [39] can be fitted in good accuracy in Fig. 4a. As shown in the circuitry, R_0 designates the solution resistance and $R_{dl}-C_{dl}$ pair stands for the capacitance (C_{dl}) and resistance (R_{dl}) of the double layer. The space charge capacitance and the charge transfer resistance are defined as C_1 and R_1 , respectively. Three parallel $R-C$ pairs, C_2 and R_2 , C_3 and R_3 , C_4 and R_4 , mean the capacitances and resistances of the discrete donor levels resulted from titanium–oxygen vacancy pairs, oxygen vacancies, and Fe^{3+} interstices, respectively. Table S1 shows the calculated model parameters of the photocatalysts based on the EIS. The sequence of the total resistance R_{total} (the summing of R_1 , R_2 , R_3 , and R_4) and the total capacitance C_{total} (the summing of C_1 , C_2 , C_3 , and C_4) of the photocatalysts is: $S_{100} < S_{50} < S_{10} < S_{200} < S_{500} < S_0$, and $S_{100} > S_{50} > S_{10} > S_{200} > S_{500} > S_0$, respectively.

The Nyquist plots of EIS data for undoped and Fe-doped TiO_2 patterned electrodes are presented in Fig. 4b. The reduced semicircles indicate decreased resistance of working electrodes in the order of S_0 , S_{500} , S_{200} , S_{10} , S_{50} , and S_{100} , which is in accordance with the results of Table S1, suggesting a decrease in the solid state interface layer resistance and the charge transfer resistance across the solid-liquid junction [40].

MS plots were performed as shown in Fig. 5 to calculate the N_d and flat-band potential (E_{fb}) of undoped and Fe-doped TiO_2 . The value of N_d listed in Table 1 can be calculated according to the MS equation [39]:

$$C_{sc}^{-2} = \left(\frac{2}{\epsilon \epsilon_0 q N_d} \right) \left(E - E_{fb} - \frac{KT}{q} \right) \quad (8)$$

where E is the applied potential, ϵ is the dielectric constant of the semiconductor, ϵ_0 is the permittivity of the vacuum, K is Boltzmann's constant, and T is the temperature (298 K). The N_d values of all photocatalysts increase from $4.74 \times 10^{18} \text{ cm}^{-3}$ at S_0 to the highest value of $9.81 \times 10^{18} \text{ cm}^{-3}$ at S_{100} , and then decrease to $5.05 \times 10^{18} \text{ cm}^{-3}$ at S_{500} with increasing doping concentration of Fe^{3+} . Therefore, it can be concluded from Table 1 and S1 that higher

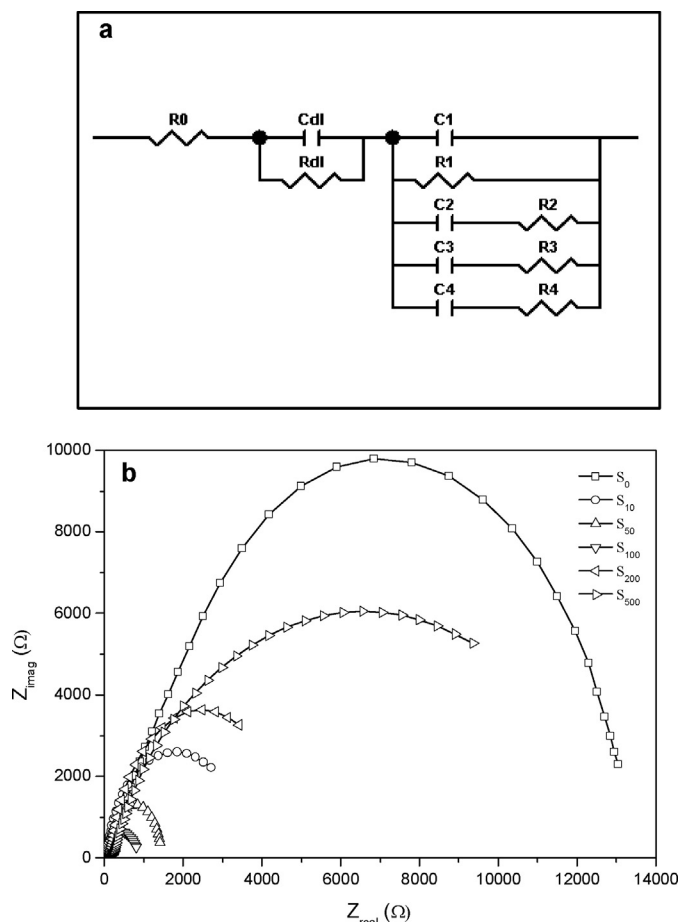


Fig. 4. (a) Suggested equivalent model and (b) Nyquist plot of undoped and Fe-doped TiO_2 electrodes under irradiation of 254 nm at open circuit potential.

N_d can lead to higher capacitance and lower resistance value of the photocatalysts.

The E_{fb} value can be obtained from the x-axis intercepts of the linear region in Fig. 5. As can be seen from MS plots, the E_{fb} of all Fe-doped TiO_2 photocatalysts are almost the same at -0.6 V vs. Ag/AgCl (equivalent to -0.4 V vs. SHE), which is compatible with previous report of TiO_2 [41]. The slopes of the line show that all Fe-doped TiO_2 nanoparticles are n -type semiconductors and

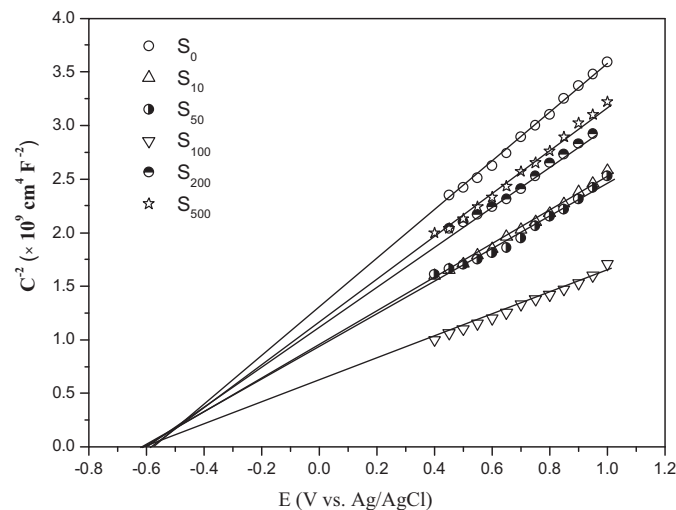


Fig. 5. MS analysis of undoped and Fe-doped TiO_2 electrodes at the potential ranging from -0.8 to 1.6 V vs. Ag/AgCl and a constant frequency of 100 Hz.

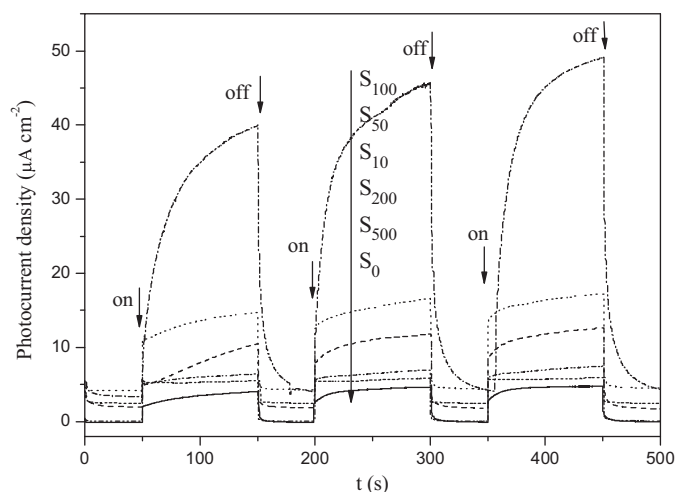


Fig. 6. Photocurrent density of undoped and Fe-doped TiO₂ electrodes with various doping concentrations of Fe³⁺ in dark and under irradiation of 254 nm.

it is generally known that the conduction band potential (E_{CB}) of n -type semiconductor is 0.1 V more negative than E_{fb} [41]. Therefore, it can be deduced that the E_{CB} of Fe-doped TiO₂ is -0.5 V vs. SHE, which is more negative than the standard redox potential of $O_2/\cdot O_2^-$ (-0.284 V vs. SHE) and N_2/NH_3 (-0.092 V vs. SHE) [42]. The valence band (VB) potential (E_{VB}) of Fe-doped TiO₂ is 2.65 V vs. SHE, which is more positive than the standard redox potential of $\cdot OH/OH^-$ (1.985 V vs. SHE) [42]. Although the standard redox potential of H_2O/H_2 is 0 V vs. SHE at pH 0 which is slightly higher than N_2/NH_3 , the reduction of N_2 to NH_3 is preferred possibly due to the overpotential of H_2 is higher than that of NH_3 on the surface of TiO₂. Actually, we did not observe the formation of H_2 in the experiments as well (data not shown). As a result, the photogenerated electrons on irradiated Fe-doped TiO₂ can reduce O_2 and N_2 to $\cdot O_2^-$ and NH_3 , respectively. Therefore, it is reasonable to conclude that photocatalytic reduction of nitrogen to ammonia on irradiated photocatalysts is chemically feasible.

To further investigate the photoinduced behavior of the generated photocurrent response of samples, the photocurrent density curves of various samples in the dark and under UV light irradiation of 254 nm were carried out as shown in Fig. 6. When the light was regularly turned on and off, a series of almost identical signals were obtained. There is a sharp increase in the photocurrent density under UV light irradiation of 254 nm. The photocurrent density of S_{100} is $40\text{--}50 \mu A cm^{-2}$, whereas that of S_0 is ca. $3 \mu A cm^{-2}$; the short-circuit photocurrent density of S_{100} is ca. 15 times higher than that of S_0 . It also proves that Fe³⁺ can provide a shallow trap for electrons and holes to inhibit the recombination of photogenerated charge carriers effectively [32].

3.3. Photocatalytic activity of Fe-doped TiO₂

Ethanol is used as an effective scavenger because the second-order rate constant for the reaction of ethanol with the hydroxyl radicals in water is $1.8 \times 10^9 M s^{-1}$ [43]. Fig. 7 shows the influence of the ethanol concentration (0, 0.008, 0.040, 0.079, 0.158, 0.395, and $0.789 g L^{-1}$) to the quantum yield using S_{100} as photocatalyst at pH 7 and 25 °C. The generated ammonia concentration and the quantum yield increase with the increasing of ethanol concentration. The ethanol with the concentration of $0.789 g L^{-1}$ exhibits the highest quantum yield of $18.27 \times 10^{-2} m^{-2}$. The nitrogen photofixation reaction does not occur when there is no ethanol present because the photogenerated holes cannot be trapped by electron donors and can be recombined with electrons quickly.

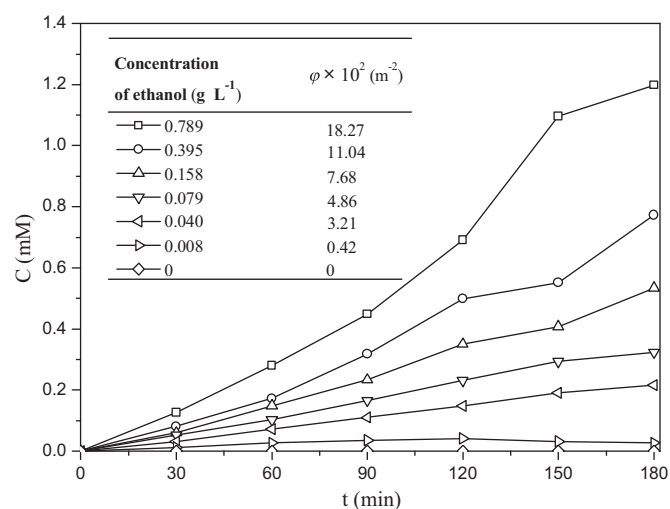


Fig. 7. Influence of the ethanol concentration to the ammonia formation using $100 \times 10^{-6} Fe^{3+}$ doped TiO₂ (S_{100}) at pH 7 and 25 °C.

Fig. 8a shows the generated ammonia concentration curves by photocatalysts with various doping concentrations of Fe³⁺ under UV light irradiation of 254 nm in the presence of $0.789 g L^{-1}$ ethanol. The generated ammonia concentration reaches more than 1.20 mM, and the quantum yield was calculated and listed in Table 1. The trends of quantum yield with doping concentration of Fe³⁺ are in agreement with the trends of PL intensity, N_d , C_{dl} , C_{total} , and photocurrent density: the highest quantum yield of $18.27 \times 10^{-2} m^{-2}$ is achieved at S_{100} , which is 3.84 times higher than S_0 . Obviously, the quantum yield increases with increasing doping concentration of Fe³⁺ and the highest value achieves at 100×10^{-6} . When the doping concentration is over 100×10^{-6} , the photocatalytic activity turns to down because Fe³⁺ gradually acts as recombination centers and the temporary photogenerated electron of hole-trapping sites disappear accordingly [37].

Fig. 8b displays the stability of the as-prepared Fe-doped TiO₂ S_{100} for nitrogen photofixation. After each run of 3 h, the photocatalytic reaction system was evacuated, and the next run was continued. There was no obvious quantum yield drop after each run, indicating the good stability of Fe-doped TiO₂ S_{100} . After 12 h of photocatalytic reaction, a quantum yield loss of only 5% was observed.

3.4. Study of $\cdot O_2^-$, $\cdot OH$, and $CH_3\dot{C}HOH$ radicals

The ESR spin-trap with 5,5-dimethyl-1-pyrroline N-oxide (DMPO) technique was performed to explore the nature of generated radicals such as $\cdot O_2^-$, $\cdot OH$, and $CH_3\dot{C}HOH$ in the nitrogen photofixation process. Fig. 9 shows the experiments results carried out in the dark and under the irradiation of 254 nm, respectively. In the presence of S_{100} , there are no signals of DMPO- $\cdot OH$, DMPO- $\cdot O_2^-$, or DMPO- $CH_3\dot{C}HOH$ observed when the reactions were performed in the dark in water, methanol, and ethanol, respectively. On the contrary, four characteristic peaks of the DMPO- $\cdot OH$, four characteristic peaks of DMPO- $\cdot O_2^-$ and six characteristic peaks of DMPO- $CH_3\dot{C}HOH$ can be observed under UV light irradiation of 254 nm when the photocatalyst was suspended in water, methanol, and ethanol, respectively [44]. These results indicate that a portion of photogenerated electrons and holes in Fe-doped TiO₂ can react with the surface adsorbed O_2 and OH^- to produce $\cdot O_2^-$ and $\cdot OH$, respectively. And, ethanol radicals $CH_3\dot{C}HOH$ [45] can be produced from the oxidation of ethanol by radicals in water like $\cdot OH$.

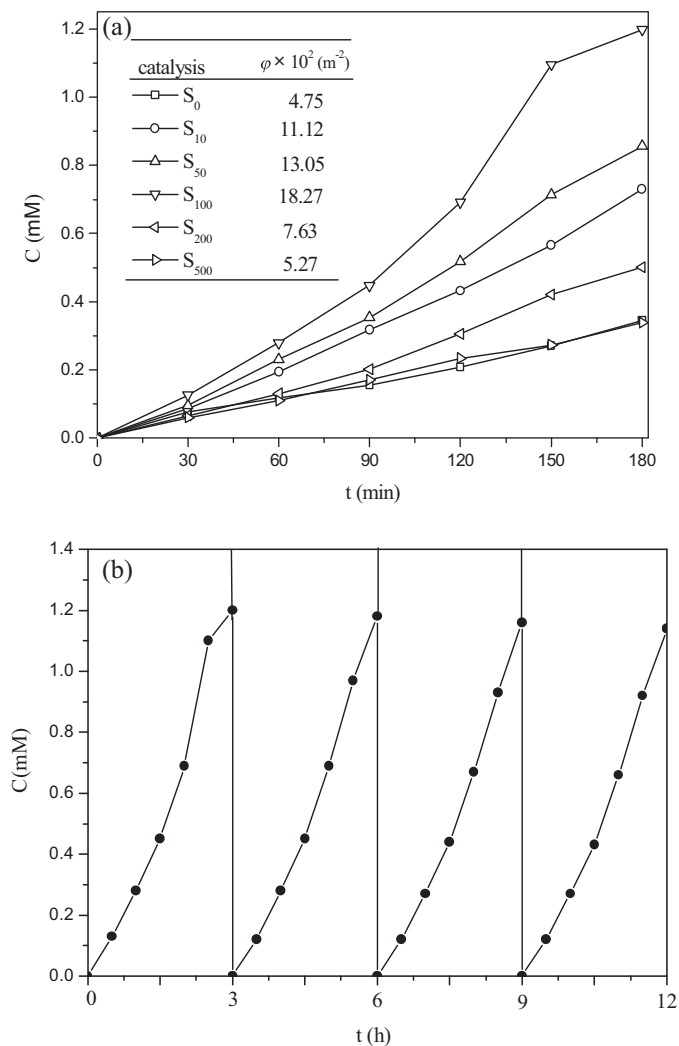


Fig. 8. Nitrogen photofixation of undoped TiO_2 and Fe-doped TiO_2 (a), and photocatalytic stability study over $100 \times 10^{-6} \text{ Fe}^{3+}$ doped TiO_2 (S_{100}) (b) in $100 \text{ mL } 0.789 \text{ g L}^{-1}$ ethanol solution under irradiation of 254 nm at $\text{pH } 7$ and 25°C .

3.5. Electron transfer mechanism in nitrogen photofixation

Fig. 10 shows a possible electron transfer mechanism of nitrogen photofixation and degradation of ethanol over photocatalysts of S_{100} in the presence of ethanol as scavenger. Under UV light irradiation, electrons e^- in the VB of Fe-doped TiO_2 can be excited to CB, and the holes h^+ can be generated in the VB (Eq. (3)) accordingly. Part of the photogenerated electrons recombine with holes in the VB, while others can be transferred to the surface of the photocatalyst to react with Fe^{3+} (Eq. (4)), O_2 (Eq. (9)), and N_2 (Eq. (10)). The unstable $\cdot\text{O}_2^-$ can be transformed to $\cdot\text{OH}$ quickly in water via Eq. (11) [46]. While the holes can be transformed to $\cdot\text{OH}$ radicals when they arrive at the surface of the photocatalyst to react with hydroxyl (Eq. (12)).

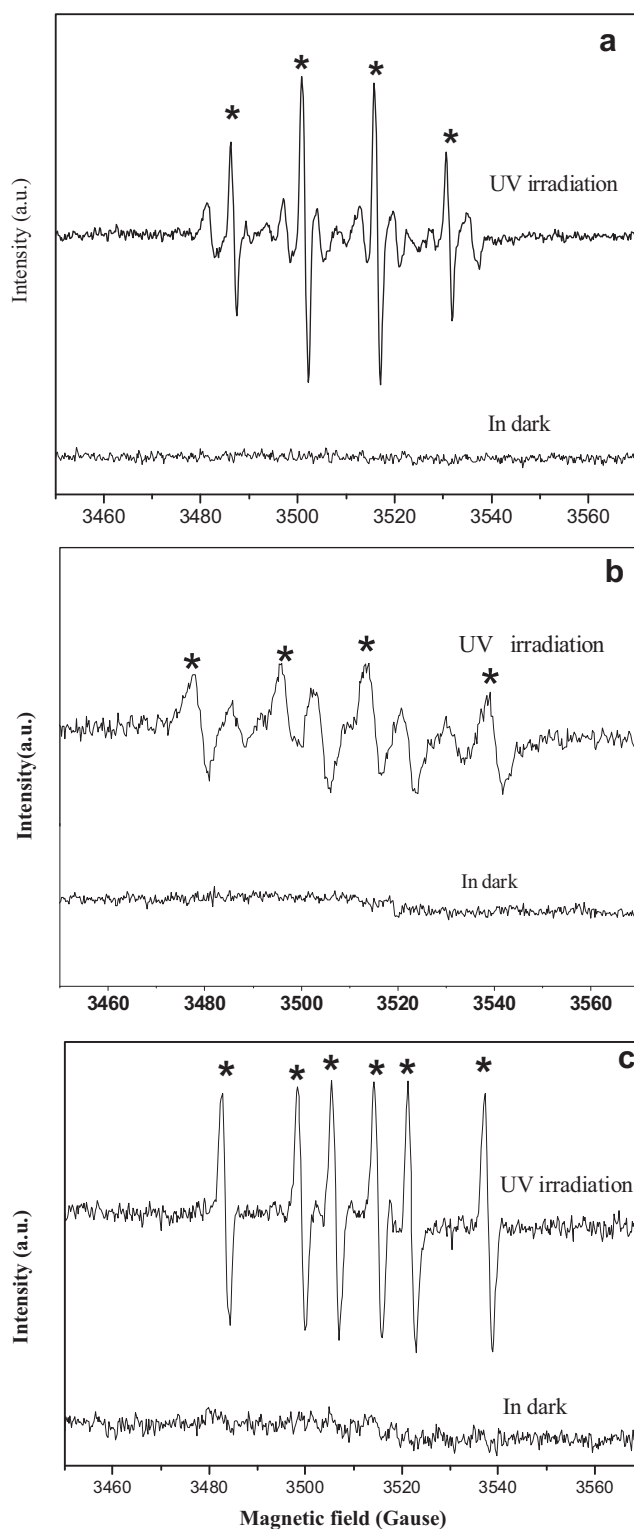
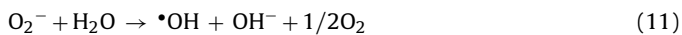
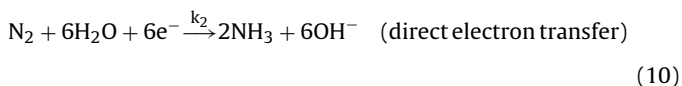


Fig. 9. DMPO spin-trapping ESR spectra of $100 \times 10^{-6} \text{ Fe}^{3+}$ doped TiO_2 (S_{100}) in dark and under UV light irradiation of 254 nm . (a) $\text{DMPO} \cdot \cdot\text{OH}$ in water, (b) $\text{DMPO} \cdot \cdot\text{O}_2^-$ in methanol, and (c) $\text{DMPO} \cdot \text{CH}_3\text{CHOH}$ in ethanol.

To further investigate the intermediates in the scavenging reaction, Nano-LC ESI Q TOF MS was used to obtain mass spectra of intermediates as shown in Fig. 11. The mass spectra clearly displays five peaks corresponding to the ion mass of Enro $[\text{NH}_2\text{NH}_2 + \text{H}]^+$ (33.0245), $[\text{NH}_2\text{OH} + \text{H}]^+$ (34.9990), $[\text{CH}_3\text{CHO} + \text{H}]^+$ (44.9990), $[\text{CH}_2 = \text{CHCHO} + \text{H}]^+$ (56.9312), and $[\text{C}_2\text{H}_5\text{OC}_2\text{H}_5 + \text{H}]^+$

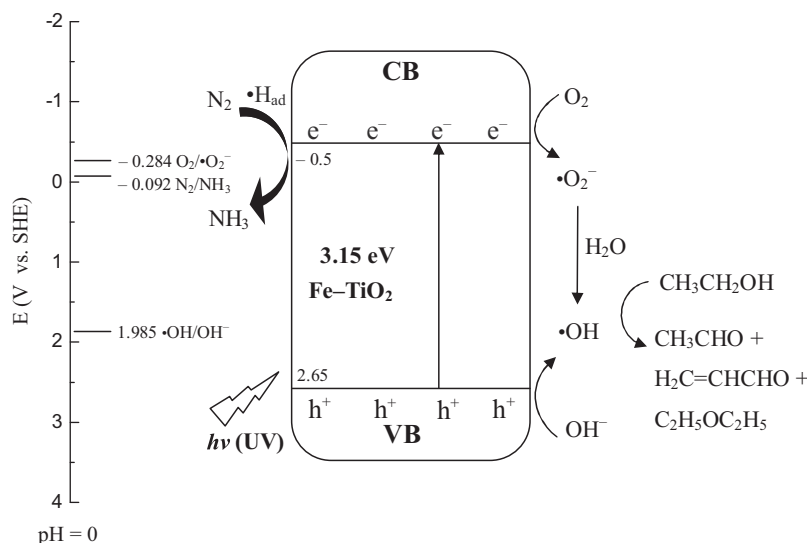


Fig. 10. Proposed mechanism of nitrogen photofixation and degradation of ethanol under UV light irradiation in the presence of ethanol as scavenger.

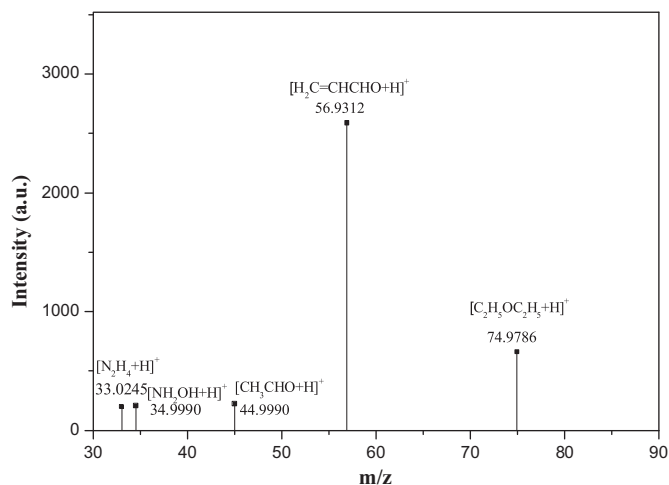
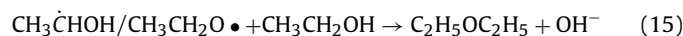
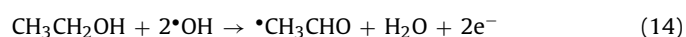
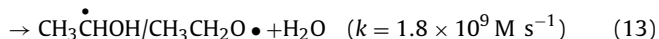
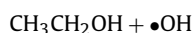


Fig. 11. Nano-LC ESI Q TOF-Mass spectra of intermediates in liquid sample.

(74.9786), respectively. Intermediates such as CH_3CHO , NH_2NH_2 , NH_2OH , $\text{CH}_2=\text{CHCHO}$, and $\text{C}_2\text{H}_5\text{OC}_2\text{H}_5$ can be determined accordingly. The concentration of hydrazine was also determined in the range of 0.34 to $1.30 \times 10^{-6} \text{ M}$ in the reaction time of 60–180 min by Pgeneral TU-1901 spectrophotometer using *p*-dimethylaminobenzaldehyde spectrophotometry method at 458 nm [47]. It is worth mentioning that there is no nitrite or nitrate formed in the process (data not shown), inferring that the ammonia cannot be oxidized to its higher oxidation states because the ethanol is an excellent $\cdot\text{OH}$ scavenger. The ethanol can be oxidized to CH_3CHO and $\text{C}_2\text{H}_5\text{OC}_2\text{H}_5$ via Eqs. (13)–(15) [43]. It is reasonable to presume that the intermediate $\text{CH}_2=\text{CHCHO}$ is produced from the condensation reaction of ethanol, intermediates, and radicals in the oxidation process although the detail pathways are not clear. NH_2OH can be attributed to the combination reaction between $\cdot\text{OH}$ and $\cdot\text{NH}_2$ formed from nitrogen reduction process, which will be discussed later on the surface of photocatalyst via Eq. (16).

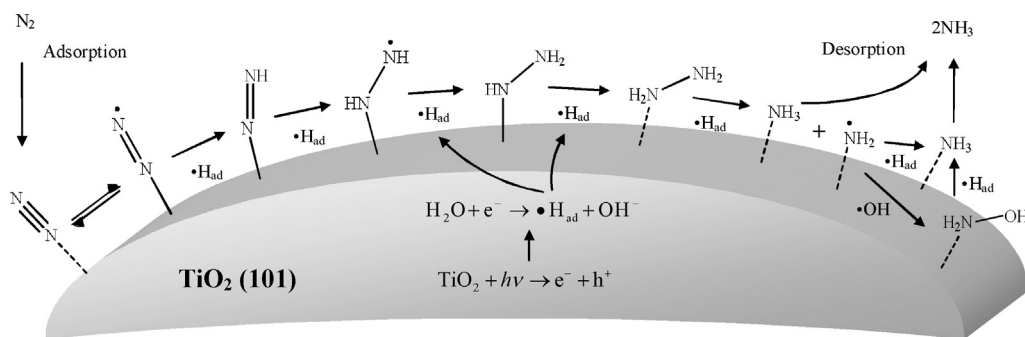


Periodic DFT was used to further investigate the transition state or intermediates in the process of N_2 photofixation on the surface of Fe-doped $\text{TiO}_2(101)$. Table 2 shows the optimized structural parameters of different nitrogen-containing adsorbate molecules calculated by DFT according to the optimized structures in Fig. S4. As shown in Table 2, the negative adsorption energies indicate that adsorption is exothermic with respect to the free adsorbate molecule. The N–Ti distances of adsorbed intermediates are between 1.937 and 2.252 Å, and the adsorption energies vary from -0.621 to -4.666 eV , indicating that the photofixation of N_2 to NH_3 process by many intermediates is relatively stable and coherent on the surface of TiO_2 . The N–N bond lengths increase from 1.183 of $\text{N}\equiv\text{N}\cdots\text{Ti}$ mode to 1.446 Å of $\text{H}_2\text{N}-\text{NH}_2\cdots\text{Ti}$ mode with the cleavages of the triple bond [48] into single bond. The $\angle\text{NNTi}$ bond angles decrease from 173.850° of $\text{N}\equiv\text{N}\cdots\text{Ti}$ mode to 104.731° of $\text{H}_2\text{N}-\text{NH}_2\cdots\text{Ti}$ mode. The adsorption configurations of N_2 and other transition states change from ‘vertical adsorption’ which one N atom points its head to Ti atom to ‘horizontal adsorption’ which the upper side N atom came close to TiO_2 surface, which is in accordance with the study of Arena’s [49].

Therefore, it can be concluded that the 1 mol N_2 can be successively reduced to 2 mol NH_3 as shown in Fig. 12 via transition state or intermediates such as $\cdot\text{N}_2=\text{N}-$ (the resonant structure of N_2), $\text{HN}=\text{N}-$, $\cdot\text{HN}-\text{NH}-$, $\text{H}_2\text{N}-\text{NH}-$, $\text{H}_2\text{N}-\text{NH}_2$, $\cdot\text{NH}_2$, and NH_2OH . The entire evolution of different adsorbate configurations in nitrogen photofixation confirms that the adsorbed H atoms ($\cdot\text{H}_{\text{ad}}$), conventional intermediates in photocatalytic hydrogen evolution process (Eq. (17)) [50], are added on N_2 successively. The electron is transferred from TiO_2 to H_2O firstly (producing $\cdot\text{H}_{\text{ad}}$), then it is imparted to adsorbates on the surface of Fe-doped TiO_2 . Comparing with $\cdot\text{NH}_2\cdots\text{Ti}$ mode, the distance of $\text{N}\cdots\text{Ti}$ at $\text{NH}_3\cdots\text{Ti}$ mode increases by 0.315 Å (from 1.937 to 2.252 Å) and the absolute values of adsorption energies decreases by 3.586 eV (from 4.666 to 1.080 eV), indicating that NH_3 can be desorbed from the surface of TiO_2 . The intermediates such as $\text{H}_2\text{N}-\text{NH}_2$ and NH_2OH in Table 2 can be also desorbed from the surface of TiO_2 as NH_3 does. By the way, the NH_2OH formed in Eq. (16) can be reduced by $\cdot\text{H}_{\text{ad}}$ to NH_3 and $\cdot\text{OH}$ as Eq. (18) as well. Therefore, the entire reduction process of 1 mol N_2

Table 2Optimized structural parameters and interaction energy of different molecules adsorbed on TiO₂(1 0 1).

Mode	N–Ti distance (Å)	N–N distance (Å)	N–N–Ti angle (°)	ΔE (eV)
N≡N...Ti	2.099	1.183	173.850	−0.621
•N=N–Ti	2.102	1.183	173.763	−0.622
HN=N–Ti	1.953	1.254	161.776	−2.599
•HN–NH–Ti	2.042	1.332	134.949	−1.589
H ₂ N–NH–Ti	1.945	1.473	127.853	−3.701
H ₂ N–NH ₂ ...Ti	2.184	1.446	104.731	−1.100
•NH ₂ ...Ti	1.937			−4.666
HONH ₂ ...Ti	2.195			−1.234
NH ₃ ...Ti	2.252			−1.080

**Fig. 12.** Successive reduction scheme from N₂ to NH₃ on the surface of TiO₂ (1 0 1).

to 2 mol NH₃ with consumption of 6 mol electrons on TiO₂ is similar to the traditional biological nitrogen fixation process [51].



3.6. Effect of oxygen on nitrogen photofixation

Because the reactions in Eqs. (4) and (6) are the electrons transfer processes inside the photocatalyst, which will not affect the relative quantity of electrons involved in the nitrogen photofixation reaction. By the assumption of steady state of electrons and ignoring the reaction of Eq. (16) due to its much lower formation rate than ammonia, the electron transfer rate in nitrogen photofixation can be described as Eq. (19) according to Eqs. (3), (9), and (10)

$$\frac{dC_{\text{e}^-}}{dt} = \phi_0 I_0 - k_1 C_{\text{e}^-}^6 P_{\text{O}_2} - k_2 C_{\text{e}^-}^6 P_{\text{N}_2} = 0 \quad (19)$$

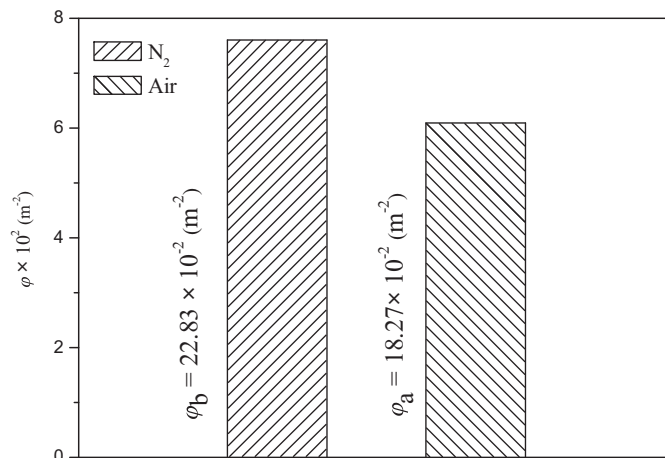
where C_{e^-} is the concentration of electrons; P_{O_2} and P_{N_2} are the partial pressure of oxygen and nitrogen in gas, k_1 and k_2 are the rate constants of Eqs. (9) and (10), respectively.

Parallel experiments were performed in pure nitrogen or air to elucidate the effect of oxygen on the nitrogen photofixation. As shown in Fig. 13, the quantum yield in air ϕ_a and pure nitrogen ϕ_b are 18.27 and $22.83 \times 10^{-2} \text{ m}^{-2}$, respectively, and the ratio of ϕ_a and ϕ_b can be calculated from experiment as 0.80.

It is clear that electrons trapped by oxygen in Eq. (9) cannot be used to reduce nitrogen to ammonia and will transformed to •OH which will eventually quenched by ethanol as depicted in Fig. 10. Thus, according to the definition of quantum yield as Eq. (1), the ratio of ϕ_a and ϕ_b can be deduced as

$$\frac{\phi_a}{\phi_b} = \frac{[k_2 C_{\text{e}^-}^6 P_{\text{N}_2}]_{\text{in air}}}{[k_2 C_{\text{e}^-}^6 P_{\text{N}_2}]_{\text{in pure N}_2}} = \frac{[P_{\text{N}_2}]_{\text{in air}}}{[P_{\text{N}_2}]_{\text{in pure N}_2}} = 0.78 \quad (20)$$

This figure is very close to the result of experiment. Thus, it can be concluded that the amount of electrons consumed by nitrogen

**Fig. 13.** Initial nitrogen photofixation rate of $100 \times 10^{-6} \text{ Fe}^{3+}$ doped TiO₂ (S₁₀₀) in pure nitrogen and air under irradiation of 254 nm in 100 mL 0.789 g L^{−1} ethanol solution at pH 7 and 25 °C.

depends on the partial pressure of nitrogen in the reaction system. Eq. (3) is the rate-determining step in the presence of ethanol as scavenger in nitrogen photofixation process comparing with the direct electron transfer of Eqs. (9) and (10). Optimal doping of Fe³⁺ plays a key role in the characteristic properties of the photocatalyst, such as inhibiting the recombination of electron–hole pairs, and enhancing charge carriers concentration, and current density, consequently improving the photocatalytic activity.

4. Conclusions

Fe-doped TiO₂ nanoparticles with highly exposed (1 0 1) facets were prepared successfully by two-step hydrothermal method, which exhibit excellent performance in nitrogen photofixation. The highest quantum yield of ammonia generated reaches $18.27 \times 10^{-2} \text{ m}^{-2}$ which is 3.84 times higher than pristine TiO₂. The results of characterizations demonstrated that Fe³⁺ ions are evenly

incorporated into the anatase crystal and substituted for Ti^{4+} in the TiO_2 lattice. Optimal doping of Fe^{3+} is of importance on the improvement of photocatalytic activity. The ESR spectra proved that the photogenerated holes and electrons were trapped by OH^- and O_2 to form $\bullet\text{OH}$ and $\bullet\text{O}_2^-$, respectively. A possible electron transfer mechanism of nitrogen photofixation over Fe-doped TiO_2 nanoparticles was proposed. The quantum yields of nitrogen photofixation depend on the partial pressure of nitrogen in the reaction. DFT calculations revealed that 1 mol N_2 can be successively converted into 2 mol NH_3 via transitional state or intermediates such as $\bullet\text{N}_2=\text{N}-$ (the resonant structure of N_2), $\text{HN}=\text{N}-$, $\bullet\text{HN}-\text{NH}-$, $\text{H}_2\text{N}-\text{NH}-$, $\text{H}_2\text{N}-\text{NH}_2$, $\bullet\text{NH}_2$, and NH_2OH on the surface of TiO_2 . The entire reduction process of 1 mol N_2 to 2 mol NH_3 with consumption of 6 mol electrons on TiO_2 is similar to the traditional biological nitrogen fixation process. In addition, the proposed electron transfer mechanism may be useful to other applications which use semiconductor materials as photocatalysts.

Acknowledgments

This work has been partially supported by National Nature Science Foundation of China (Grant Nos. 51178412 and 51278456), and Zhejiang Provincial Education Department Scientific Research Projects (Grant No. Z201122663).

Appendix A. Supplementary data

Supplementary data associated with this article can be found, in the online version, at <http://dx.doi.org/10.1016/j.apcatb.2013.07.047>.

References

- [1] K. Hoshino, *Chemistry: A European Journal* 7 (2001) 2727–2731.
- [2] K. Hoshino, R. Kuchii, T. Ogawa, *Applied Catalysis A* 79 (2008) 81–88.
- [3] O. Rusina, O. Linnik, A. Eremenko, H. Kisch, *Chemistry: A European Journal* 9 (2003) 561–565.
- [4] G.N. Schrauzer, T.D. Guth, *Journal of the American Chemical Society* 99 (1977) 7189–7193.
- [5] M.M. Khader, N.N. Lichten, G.H. Vurens, M. Salmeron, G.A. Somorjai, *Langmuir* 3 (1987) 303–304.
- [6] L. Palmisano, V. Augugliaro, A. Sclafani, M. Schiavello, *Journal of Physical Chemistry* 92 (1988) 6710–6713.
- [7] J. Soria, J.C. Conesa, V. Augugliaro, L. Palmisano, M. Schiavello, A. Sclafani, *Journal of Physical Chemistry* 95 (1991) 274–282.
- [8] W. Dai, X. Wang, P. Liu, Y. Xu, G. Li, X. Fu, *Journal of Physical Chemistry B* 110 (2006) 13470–13476.
- [9] O. Linnik, H. Kisch, *Photochemical and Photobiological Sciences* 5 (2006) 938–942.
- [10] M. Lazzeri, A. Vittadini, A. Selloni, *Physical Review B* 63 (2001) 155409.
- [11] U. Diebold, N. Ruzsicki, G.S. Herman, A. Selloni, *Catalysis Today* 85 (2003) 93–100.
- [12] Q.J. Xiang, J.G. Yu, M. Jaroniec, *Chemical Communications* 47 (2011) 4532–4534.
- [13] J. Pan, G. Liu, G.M. Lu, H.M. Cheng, *Angewandte Chemie International Edition* 50 (2011) 2133–2137.
- [14] F. Amano, T. Yasumoto, O.O. Prieto-Mahoney, S. Uchida, T. Shibayama, B. Ohtani, *Chemical Communications* (2009) 2311–2313.
- [15] Y.F. Li, Z.P. Liu, *Journal of the American Chemical Society* 133 (2011) 15743–15752.
- [16] Z. Xiong, X.S. Zhao, *Journal of the American Chemical Society* 134 (2012) 5754–5757.
- [17] N. Wu, J. Wang, N. Tafen de, H. Wang, J.G. Zheng, J.P. Lewis, X. Liu, S.S. Leonard, A. Manivannan, *Journal of the American Chemical Society* 132 (2010) 6679–6685.
- [18] D. Kuang, J.r.m. Brillet, P. Chen, M. Takata, S. Uchida, H. Miura, K. Sumioka, S.M. Zakeeruddin, M. Gratzel, *ACS Nano* 2 (2008) 1113–1116.
- [19] H.H. Ou, C.H. Liao, Y.H. Liou, J.H. Hong, S.L. Lo, *Environmental Science and Technology* 42 (2008) 4507–4512.
- [20] S.U.M. Khan, J. Akikusa, *Journal of Physical Chemistry B* 103 (1999) 7184–7189.
- [21] J.P. Perdew, K. Burke, M. Ernzerhof, *Physical Review Letters* 77 (1996) 3865–3868.
- [22] V. Milman, B. Winkler, J.A. White, C.J. Pickard, M.C. Payne, E.V. Akhmatkaya, R.H. Nobes, *International Journal of Quantum Chemistry* 77 (2000) 895–910.
- [23] Y. Yalcin, M. Kilic, Z. Cinar, *Applied Catalysis B* 99 (2010) 469–477.
- [24] J. Yu, Q. Xiang, M. Zhou, *Applied Catalysis B* 90 (2009) 595–602.
- [25] J. Zhu, F. Chen, J. Zhang, H. Chen, M. Anpo, *Journal of Photochemistry and Photobiology A* 180 (2006) 196–204.
- [26] T. Tong, J. Zhang, B. Tian, F. Chen, D. He, *Journal of Hazardous Materials* 155 (2008) 572–579.
- [27] K. Nagaveni, M.S. Hegde, G. Madras, *Journal of Physical Chemistry B* 108 (2004) 20204–20212.
- [28] H. Shi, H. Wang, J.H. Xin, X. Zhang, D. Wang, *Chemical Communications* 47 (2011) 3825–3827.
- [29] Z.W. Liu, C.K. Ong, T. Yu, Z.X. Shen, *Applied Physics Letters* 88 (2006) 053110–053113.
- [30] Y. Yang, X. Wang, C. Sun, L. Li, *Journal of Applied Physics* 105 (2009) 094304–094305.
- [31] H. Nakajima, H. Ishihara, Q. Shen, T. Toyoda, K. Itoh, H. Kaneko, Y. Tamaura, *Journal of Alloys and Compounds* 441 (2007) 255–258.
- [32] J. Yu, H. Yu, B. Cheng, X. Zhao, Q. Zhang, *Journal of Photochemistry and Photobiology A* 182 (2006) 121–127.
- [33] Z.J. Li, W.Z. Shen, W.S. He, X.T. Zu, *Journal of Hazardous Materials* 155 (2008) 590–594.
- [34] J.G. Yu, H.G. Yu, C.H. Ao, S.C. Lee, J.C. Yu, W.K. Ho, *Thin Solid Films* 496 (2006) 273–280.
- [35] N. Serpone, *Journal of Physical Chemistry B* 110 (2006) 24287–24293.
- [36] N.D. Abazovic, L. Mirengi, I.A. Jankovic, N. Bibic, D.V. Sojic, B.F. Abramovic, M.I. Comor, *Nanoscale Research Letters* 4 (2009) 518–525.
- [37] M.H. Zhou, J.G. Yu, B. Cheng, *Journal of Hazardous Materials* 137 (2006) 1838–1847.
- [38] Y.L. Pang, A.Z. Abdullah, *Applied Catalysis B* 129 (2013) 473–481.
- [39] N. Baram, Y. Ein-Eli, *Journal of Physical Chemistry C* 114 (2010) 9781–9790.
- [40] Y. Zhang, N. Zhang, Z.R. Tang, Y.J. Xu, *Physical Chemistry Chemical Physics* 14 (2012) 9167–9175.
- [41] H. Huang, D. Li, Q. Lin, Y. Shao, W. Chen, Y. Hu, Y. Chen, X. Fu, *Journal of Physical Chemistry C* 113 (2009) 14264–14269.
- [42] A.J. Bard, R. Parsons, J. Jordan, *Standard Potentials in Aqueous Solution*, Marcel Dekker, New York, 1985.
- [43] M.S. Matheson, A. Mamou, SilvermaJ., J. Rabani, *Journal of Physical Chemistry* 77 (1973) 2420–2424.
- [44] M. Sun, D. Li, Y. Chen, W. Chen, W. Li, Y. He, X. Fu, *Journal of Physical Chemistry C* 113 (2009) 13825–13831.
- [45] G. Czapski, J. Holcman, B.H.J. Bielski, *Journal of the American Chemical Society* 116 (1994) 11465–11469.
- [46] K. Nagaveni, M.S. Hegde, N. Ravishankar, G.N. Subbanna, G. Madras, *Langmuir* 20 (2004) 2900–2907.
- [47] G.W. Watt, J.D. Chrisp, *Analytical Chemistry* 24 (1952) 2006–2008.
- [48] D.J. Arp, L.Y. Stein, *Critical Reviews in Biochemistry and Molecular Biology* 38 (2003) 471–495.
- [49] F. Arena, F. Ferrante, L. Spadaro, A. Prestianni, A. Raneri, D. Duca, *Journal of Physical Chemistry C* 115 (2011) 24728–24733.
- [50] Q. Gu, X. Fu, X. Wang, S. Chen, D.Y.C. Leung, X. Xie, *Applied Catalysis B* 106 (2011) 689–696.
- [51] B.M. Hoffman, D.R. Dean, L.C. Seefeldt, *Accounts of Chemical Research* 42 (2009) 609–619.